

Yuh, I., and Day, J.M.D., 2023, Previously melt-depleted mantle beneath the Cascades Range arc: *Geology*, <https://doi.org/10.1130/G51376.1>

## Supplemental Material

**Samples and Analytical Methods.**

**Figures S1–11.**

**Tables S1–S10.**

## SUPPLEMENTARY INFORMATION

## Previously melt-depleted mantle beneath the Cascades Range arc

### SAMPLES AND ANALYTICAL METHODS

Geochemical data are reported for 11 spinel harzburgite xenoliths, 16 trachybasaltic tephra representing host lavas, one trachybasaltic lava flow, and two crustal xenoliths. Samples were collected from Lorena Butte except for two trachybasalts collected at Blockhouse Butte (**Figures S1, S2**). Eight of the studied tephra from Lorena Butte hosted peridotite xenoliths, and one hosted a crustal xenolith. Samples were prepared by cutting into blocks using a diamond-tipped rotary saw, crushed using an alumina-plated jaw crusher, and powdered using an alumina shatter box.

#### *Electron probe microanalysis (EPMA)*

Polished thin sections were made for nine harzburgite xenoliths, and olivine, spinel, orthopyroxene, and minor clinopyroxene were analyzed for major- and minor-element compositions using a JEOL JXA-8900 electron probe microanalyzer equipped with four wavelength dispersive X-ray spectrometers at the University of Nevada Las Vegas. An acceleration potential of 15 kV and a beam current of 10 nA were used, with the beam focused to 2  $\mu\text{m}$ . At least four separate spots for each mineral phase were analyzed, except for clinopyroxene due to its low modal abundance in harzburgites. Count times of 30 seconds (peak) and 15 seconds (background) were utilized for each element. Standards run for olivine, pyroxene, and spinel are listed in the *Supplementary Tables*.

#### *Major- and trace-element abundances analyses*

Whole-rock major element concentrations were done using X-ray fluorescence (XRF) analysis using a PANalytical 2404 X-ray fluorescence vacuum spectrometer at Franklin and Marshall College, Lancaster, PA, following methods outlined in [Boyd and Mertzman \(1987\)](#) and [Mertzman \(2000\)](#). Samples were heated to determine loss on ignition (LOI) prior to rock powder being mixed with lithium tetraborate, placed in a platinum crucible and heated with a Meker burner until molten. The molten material was then transferred to a platinum casting dish and quenched. This procedure produces a glass disk that is then used for XRF analysis. Typical accuracy of the analyses was ~1% for major elements for concentrations >0.5%. Major and minor elements in concentrations <0.5% had an accuracy of ~5%. Working curves for each element were determined by analyzing geochemical rock standards outlined in [Abbey \(1983\)](#), [Govindaraju \(1994\)](#), and [Mertzman \(2000\)](#). Compositions of  $\text{Fe}^{3+}$  and  $\text{Fe}^{2+}$  were calculated from the total measured FeO based on stoichiometry ([Droop, 1987](#)). Precision and accuracy are estimated using repeat analyses of standards, with long-term reproducibility (in wt. % and  $2\sigma$  absolute standard deviation,  $n = 13$ ) of  $\pm 0.13$  for  $\text{SiO}_2$ ,  $\pm 0.01$  for  $\text{TiO}_2$ ,  $\pm 0.09$  for  $\text{Al}_2\text{O}_3$ ,  $\pm 0.63$  for FeO,  $\pm 0.47$  for  $\text{Fe}_2\text{O}_3$ ,  $\pm 0.10$  for  $\text{Fe}_2\text{O}_3^{\text{T}}$ ,  $\pm 0.01$  for MnO,  $\pm 0.04$  for MgO,  $\pm 0.07$  for CaO,  $\pm 0.03$  for  $\text{Na}_2\text{O}$ ,  $\pm 0.01$  for  $\text{K}_2\text{O}$ , and  $\pm <0.01$  for  $\text{P}_2\text{O}_5$ . Accuracy for the average of 13 runs of BHVO-2 relative to USGS values is better than 0.2% for  $\text{SiO}_2$  and  $\text{TiO}_2$ , <1% for  $\text{Al}_2\text{O}_3$ , MgO,  $\text{Fe}_2\text{O}_3^{\text{T}}$ , CaO,  $\text{Na}_2\text{O}$ ,  $\text{P}_2\text{O}_5$ , and <3% for  $\text{K}_2\text{O}$  ([Day et al., 2017](#)). Elemental Rb, Sr, Zr, V, Cr, Ba were measured by both ICP-MS and XRF with generally 1:1 correlation, but ICP-MS measurements of these elements were preferred due to the higher sensitivity of the technique.

Whole-rock powders were measured for trace-element abundances at the Scripps Isotope Geochemistry Laboratory (SIGL). Samples were digested at 150°C in Optima grade concentrated HF (4 mL) and HNO<sub>3</sub> (1 mL) for >72 hrs on a hotplate, with total analytical blanks, and terrestrial basalt standards. Samples were sequentially dried and taken up in concentrated HNO<sub>3</sub> to remove fluorides, followed by dilution and doping with a 1 ppm indium solution to monitor instrumental drift during analysis. Trace-element abundance analyses were done using a *ThermoScientific* iCAP Qc quadrupole ICP-MS in standard mode. Analyses were standardized versus reference material BHVO-2 that was measured throughout the analytical run. In addition, reference materials were analyzed as “unknowns” (BHVO-2, BIR-1, BCR-2 and AGV-2) to assess matrix matching, external reproducibility, and accuracy. For trace-elements, reproducibility of the reference materials was generally better than 5% (RSD), except for B (24% RSD), S (34% RSD), and Zn (10% RSD; *Supplementary Tables*). Reproducibility is in line with standard reference material data reported previously for the laboratory (e.g., [Day et al., 2017](#)).

### ***Osmium isotope and highly siderophile element abundance analyses***

Osmium isotope and the highly siderophile element (HSE) abundance analyses were performed at the *SIGL*. Precisely weighed homogenized powders were digested in sealed borosilicate Carius tubes with isotopically enriched spikes and a 1:2 mixture of Teflon distilled 10M HCl and 14M HNO<sub>3</sub> purged of excess Os by treatment and reaction with H<sub>2</sub>O<sub>2</sub>. Samples were digested in the oven at 270°C for 72 hours. Osmium was triply extracted using CCl<sub>4</sub> then back-extracted into HBr ([Cohen & Waters, 1996](#)) before purification by a modified double micro-distillation procedure ([Birck et al., 1997](#)). Remaining HSE were recovered from the residual solution using standard anion exchange techniques ([Day et al., 2016](#)).

Osmium isotope compositions were measured using a *ThermoScientific* Triton thermal ionization mass spectrometer in negative mode (N-TIMS). Rhenium, Pd, Pt, Ru, and Ir were measured using a *Cetac* Aridus II desolvating nebulizer coupled to an iCAPQc ICP-MS. Offline corrections for Os involved an oxide correction, an iterative fractionation correction using  $^{192}\text{Os}/^{188}\text{Os} = 3.08271$ , a  $^{190}\text{Os}$  spike subtraction, and finally, an Os blank subtraction. Precision for  $^{187}\text{Os}/^{188}\text{Os}$ , determined by measurement of the UMCP Johnson-Matthey standard run in the same magazines as samples was better than 0.2% (UMCP 35pg =  $0.11377 \pm 0.00025$ , n = 9). Rhenium, Ir, Pt, Pd and Ru isotopic ratios for sample solutions were corrected for mass fractionation using the deviation of the standard average run on the day over the natural ratio for the element. External reproducibility on HSE analyses was better than 0.5% for 0.5 ppb solutions and all reported values are blank corrected. True reproducibility on peridotite samples is given by repeat analysis of reference materials such as MUH-1 and HARZ-01, with data for these samples from the SIGL reported in [Day et al. \(2016\)](#) and [Snortum & Day \(2020\)](#). The total procedural blank run with the samples had  $^{187}\text{Os}/^{188}\text{Os} = 0.16 \pm 0.13$  with quantities (in picograms) of 20 [Re], 8 [Pd], 12 [Pt], 140 [Ru], 2.5 [Ir], and 0.25 [Os]. These blanks are similar to or slightly higher compared to those run recently in the laboratory (e.g., [Snortum & Day, 2020](#)) and relate either to the new batch of Carius tubes used, where the batch of Pyrex used can be a strong contaminant for the HSE (e.g., [Day & Walker, 2015](#)), or during minor cross-contamination during column chemistry. Nonetheless, for most samples blank corrections were minor for Pd, Pt, and Ir at less than 2%, apart from Pt in LB2007X (88% blank contribution) and were below 8% for Ru except for LB2012L (58% blank contribution). Rhenium blank contributions ranged between 17 and 47%.

### ***Geothermometry and oxygen fugacity***

Equilibrium temperatures for the harzburgite xenoliths were estimated to be between 962 to 1070°C based on the two-pyroxene geothermometer of [Brey & Kohler \(1990\)](#). The olivine-spinel geothermometer of [Jianping et al. \(1995\)](#) and Ca-in-opx geothermometer of [Brey & Kohler \(1990\)](#) were also used for comparison. Oxygen fugacity was calculated using equation 4 in [Davis et al. \(2017\)](#) following [Mattioli & Wood \(1988\)](#) and [Wood & Virgo \(1989\)](#):

$$\log fO_2 = \frac{-24222}{T} + 8.64 + \frac{0.0567P}{T} - 12 \log(1 - \text{Mg\#}_{\text{Ol}}) - \frac{2620}{T} (\text{Mg\#}_{\text{Ol}})^2 + 3 + 2\log(\alpha_{\text{Fe}_3\text{O}_4}^{\text{Spl}})$$

where  $P$  is pressure in bars,  $T$  is temperature in Kelvins,  $\text{Mg\#}_{\text{Ol}}$  is the Mg-number in olivine ( $\text{Mg-number} = \text{Mg}/[\text{Mg}+\text{Fe}]$ ),  $X_{\text{Fe}}^{\text{M1}}$  and  $X_{\text{Fe}}^{\text{M2}}$  are the mole fractions of Mg and Fe in two orthopyroxene octahedral sites calculated following [Wood & Banno \(1973\)](#), and  $\alpha_{\text{Fe}_3\text{O}_4}^{\text{Spl}}$  is the activity of the magnetite component in spinel calculated using the MELTS Supplemental Calculator ([Sack & Ghiorso, 1991a, 1991b](#); <https://melts.ofm-research.org/CalcForms/index.html>). Pressure is assumed to be 15 kbar, approximately in the middle of the spinel stability field, following [Wood et al. \(1990\)](#) and [Brandon & Draper \(1996\)](#). Calculations of temperature and oxygen fugacity are shown in Table S9.

Oxygen fugacity is reported relative to the fayalite-magnetite-quartz (FMQ) buffer parameterized by [Frost \(1991\)](#):

$$\log fO_2(\text{FMQ}) = \frac{-25096.3}{T} + 8.735 + \frac{0.11(P - 1)}{T}$$

Using the [Brey & Kohler \(1990\)](#) two-pyroxene geothermometer, the calculated  $fO_2$  ranges from 0.2 to 1.5 log units above the fayalite-magnetite-quartz buffer (FMQ). The [Wood & Virgo \(1989\)](#) correction procedure for  $\text{Fe}^{3+}/\Sigma\text{Fe}$ , which improves the accuracy of the calculations, was not applied because Mossbauer spectroscopy was not conducted for this study. Hence, the uncertainty is roughly 0.5 log units of  $fO_2$ , with calculated temperatures representing the parameter with the largest possible source of error. These values compare favorably to those previously reported by [Brandon & Draper \(1996\)](#) using the two-pyroxene geothermometer of [Brey & Kohler \(1990\)](#) and the  $fO_2$  formulation of [Wood & Virgo \(1989\)](#): 0.3 to 1.4 log units above FMQ, with an uncertainty of 0.4 to 0.5 log units. Compared to the  $fO_2$  formulation of [Wood & Virgo \(1989\)](#), the  $fO_2$  formulation of [Davis et al. \(2017\)](#) used in this study results in  $fO_2$  values that are approximately 0.3 log units higher ([Birner et al., 2018](#)). This is within the uncertainty of the measurement, however, so does not significantly alter the  $fO_2$  estimates.

## DETAILED RESULTS

### *Petrography of mantle xenoliths*

Eight mantle xenoliths, measured for HSE abundances, Re-Os isotopes and  $fO_2$ , are shown in **Figure S3**. Samples are generally characterized by protogranular textures with between 47 and 83 modal % olivine, with grains between ~0.5 to up to 5 mm, 15-50 modal % orthopyroxene between ~0.5 up to patches of 7 mm, trace to up to 2 modal% clinopyroxene, and between 0.7 to 4 modal% spinel generally less than 1 mm, and typically 0.25-0.5 mm in maximum dimensions. Sulfide grains are rare or absent in the polished thin-sections. Sample LB2015X has a sheared textural appearance with elongated olivine. Several of the polished thin-sections of the xenoliths show evidence for host-melt and xenolith interaction, and this is particularly notable for LB2019X.

### *Major and trace element abundances in host lavas*

Major element variations in the Lorena Butte trachybasalts span a relatively narrow range of MgO (5.2 to 6.7 wt. %), TiO<sub>2</sub> (2.16 to 2.31 wt. %), Al<sub>2</sub>O<sub>3</sub> (16.0 to 16.8 wt. %), Fe<sub>2</sub>O<sub>3</sub><sup>T</sup> (11.6 to 12.0 wt. %), CaO (6.3 to 6.6 wt. %), Na<sub>2</sub>O (4.06 to 4.75 wt. %), and K<sub>2</sub>O (2.15 to 2.39 wt. %), and have low loss on ignition (-0.2 to 1.1 wt. %) (**Figure S4**). Two Blockhouse Butte trachybasalts—one scoria (BH2030L) and one lava flow (BH2032L)—have similar major element compositions, with MgO, TiO<sub>2</sub>, and Na<sub>2</sub>O in the field of Lorena Butte lavas within analytical uncertainty but slightly elevated CaO (6.84 wt. %) and lower K<sub>2</sub>O (2.02 to 2.06 wt. %). Loss on ignition is similarly low (~0.2 wt. %). Incompatible trace elements range from ~4 × Primitive Mantle (PM) to ~100 × PM, with relative enrichment generally increasing with incompatibility. Exceptions to this trend are strong relative depletions in Cs and Pb in most samples, moderate relative depletions in Rb, Th, and U, and a slight relative enrichment in Sr. No relative depletion is observed for Nb and Ta, which suggests limited subduction influence on the lavas (**Figure S5**). The REE patterns display a narrow range of variation among samples and show a decreasing trend with increasing compatibility from La ~70 × PM to Lu ~4 × PM. The two Blockhouse Butte samples, though following the same trends, are generally slightly less enriched than those of Lorena Butte and show stronger depletions in Cs, U, and Pb. Lorena Butte and Blockhouse Butte lie within the main field of compositions reported previously for volcanic rocks of the Simcoe Volcanic Field (e.g., **Figure S4**)

#### ***Major and trace element abundances in crustal xenoliths***

Major element variations in the two crustal xenolith samples differ considerably. Sample LB2020C—a mafic granulite—has major element abundances that closely match those of the lavas in MgO (5.4 wt. %), TiO<sub>2</sub> (2.12 wt. %), Al<sub>2</sub>O<sub>3</sub> (16.0 wt. %), Fe<sub>2</sub>O<sub>3</sub><sup>T</sup> (11.2 wt. %), CaO (6.37 wt. %), Na<sub>2</sub>O (4.09 wt. %), and K<sub>2</sub>O (2.18%). In contrast, sample LB2023C has elevated SiO<sub>2</sub> (82.9 wt. %) and low MgO (1.2 wt. %), TiO<sub>2</sub> (0.21 wt. %), Al<sub>2</sub>O<sub>3</sub> (11.5 wt. %), Fe<sub>2</sub>O<sub>3</sub><sup>T</sup> (1.56 wt. %), CaO (0.63 wt. %), Na<sub>2</sub>O (0.99 wt. %), and K<sub>2</sub>O (0.92 wt. %). Loss on ignition was 0.53 and 0.99 wt. %, respectively, for LB2020C and LB2023C. For the crustal xenoliths, the incompatible trace element variation of LB2020C mirrors that of the trachybasalts. Sample LB2023C is generally more enriched relative to the lavas with the incompatible trace elements ranging from ~5 × PM to ~200 × PM, except for strong depletions in K, Sr, and Ti, and moderate depletions in Rb, Ba, Nb, Ta, Pb, Zr, and Eu (**Figure S6**). The REE pattern show a decreasing trend with increasing compatibility from La ~120 × PM to Lu ~20 × PM, with a depletion in Eu.

#### ***Major and trace element abundances in harzburgites***

Major element concentrations in the studied Lorena Butte harzburgite xenoliths are similar to those previously reported in the literature ([Brandon & Draper, 1996](#)) and to abyssal harzburgites ([Day et al., 2017](#)) and are consistent with the harzburgites experiencing significant melt depletion (**Figure S7**). The harzburgites span a range of MgO of 42.6 to 44.0 wt.%, Al<sub>2</sub>O<sub>3</sub> of 0.98 to 2.46 wt. %, Fe<sub>2</sub>O<sub>3</sub><sup>T</sup> of 8.22 to 9.94 wt. %, and CaO of 0.44 to 1.30 wt. %. Negative loss of ignition for the harzburgites (-0.6 to -0.1%) corresponds with visual evidence for little to no alteration in samples. Harzburgites have a high concentration of compatible trace elements (Cr 2260 to 4010 µg/g, Ni 2270 to 2430 µg/g, Co 113 to 130 µg/g) relative to host trachybasalts (Cr 99 to 142 µg/g, Ni 78.3 to 108 µg/g, Co 31.7 to 39.5 µg/g). For the harzburgites, the normalized abundances of incompatible trace elements range from ~0.02 to ~10 times primitive mantle (PM) abundances, and the plot is characterized by a sublinear trend just under PM concentration for the most incompatible elements, a slight decreasing trend for moderately incompatible elements, and an



increasing trend for the least incompatible elements. The overall inflection pattern of the plot mirrors that of the trachybasalts. Trace elements displaying the most variability are Pb, U, K, Cs, Sr, Ba—generally large ion lithophile and/or fluid mobile elements. Harzburgite LB2007X displays an anomalously strong enrichment in K ( $5 \times \text{PM}$ ), whereas other harzburgites are at or below PM-values, and LB2015X is distinctively more enriched in REE compared to other samples. The REE trend for the harzburgites generally displays a concave-up pattern, with light REE just under  $1 \times \text{PM}$ , moderate REE depletion of near  $0.1 \times \text{PM}$ , and a slight increase in heavy REE relative to MREE (**Figure S8**).

Trace element variations in the Lorena Butte harzburgite xenoliths differ significantly from those of abyssal harzburgites (e.g., Day et al., 2017). The Lorena Butte harzburgites generally display near-PM concentrations of incompatible trace elements, whereas abyssal harzburgites are depleted in incompatible trace elements because of melt extraction (e.g., Becker & Dale, 2016; Day et al., 2017). The relative enrichment of incompatible trace elements in the Lorena Butte harzburgites compared to the melt-depleted upper mantle can be explained by metasomatic processes involving slab-derived fluids or melts typical within a subduction setting (e.g., Brandon et al., 1996, Downes, 2001).

### ***Highly siderophile element (HSE) abundances and osmium isotope systematics***

The HSE (Os, Ir, Ru, Pt, Pd, Re) concentrations and Os isotope systematics of one trachybasalt and 10 harzburgites are reported in the *Supplementary Tables*. The trachybasalt has a  $^{187}\text{Os}/^{188}\text{Os}$  of 0.1430 with an Os concentration of 0.017 ng/g. It displays near-PM concentrations for the relatively incompatible Re and Pd and is moderately depleted ( $\sim 0.01 \times \text{PM}$ ) for Pt and the compatible HSE (Os, Ir, Ru). The  $^{187}\text{Os}/^{188}\text{Os}$  of the harzburgites ranges from 0.1212 to 0.1246 with a mean of 0.1231 ( $n = 10$ ,  $2 \text{ SD} = 0.0020$ ), which is near the center of the fields for OIB xenoliths (mean = 0.1244) and abyssal peridotites (mean = 0.1243; Becker & Dale, 2016). This average is less radiogenic than the values reported in Brandon et al., 1996; 1999) (**Figure S9**).

Harzburgites exhibit variable concentrations of Os (0.233 to 4.91 ng/g), Ir (0.502 to 3.71 ng/g), Ru (1.87 to 6.46 ng/g), Pt (0.002 to 6.07 ng/g), Pd (0.111 to 2.30 ng/g) and Re (0.030 to 0.083 ng/g). In general, the PM-normalized HSE trends ranging from  $\sim 0.01$  to 1 times PM values and compare with abyssal peridotites except for lower concentrations of the moderately incompatible Re and slightly incompatible Pd in the Lorena Butte harzburgites. Notably, sample LB2007X is highly depleted in Pt ( $0.0003 \times \text{PM}$ ). Variations in the HSE patterns for the peridotites are likely caused by the “nugget effect” resulting from heterogeneous distribution of trace HSE-rich phases in peridotites (e.g., Becker & Dale, 2016). This effect can be reduced if sufficiently large whole-rock samples are prepared and well-mixed. A possible explanation for strong depletion of Pt observed in LB2007X is destabilization of a preexisting Pt-alloy causing Pt to be released into the melt (Secchiari et al., 2020). This Pt-depletion is observed in some ophiolitic mantle peridotites from New Caledonia (Secchiari et al., 2020) and further suggests heterogeneous fluid flow within the mantle section at a small scale (Snortum & Day, 2020). Parameters of HSE modelling in Fig. 1b are given in Table S10.

### ***Lorena Butte volcanic stratigraphy and melt chemistry***

Rising approximately 100 meters in height above the surrounding topography, Lorena Butte is one of  $\sim 25$  Pleistocene scoria cones that superimpose a Pliocene shield-like edifice in the southern section of the volcanic field (**Figure S10**). This edifice formed and extruded through the mid-Miocene Wanapum member of the Columbia River Basalt Group (CRBG) and consists

mostly of mafic flows and vents but has a largely rhyolitic core (Hildreth & Fierstein, 2015). Previous K-Ar dating yielded ages ranging from 2 Ma to 600 ka across the scoria cones located in the southern section of the volcanic field (Uto et al., 1991; Hildreth & Fierstein, 2015). A significant portion of the eastern half of Lorena Butte has been quarried for commercial use, exposing minimally weathered scoria, crustal xenoliths, and peridotite xenoliths. Samples were collected stratigraphically upward from near the center of the cone. Approximately 15 meters of vertical section was sampled, limited by safety and accessibility in the quarry. In the section sampled, the strata alternated between scoriaceous tephra containing a high (>40%) proportion and a low (<20%) proportion of 10-cm to 1-m-sized vesiculated blocks and bombs. Both strata hosted various xenolith species. The color of the scoria ranged from brown to dark gray to red moving up section, reflecting a change in oxidation near the vent.

The alternating strata containing different proportions of volcanic blocks suggest that the vent activity shifted between Hawaiian and Strombolian eruptive styles. However, no significant chemical variation is observed across the studied section of the cone despite changes in stratigraphy. Major- and trace-element trends show no correlation with respect to stratigraphy and display little overall variability between samples except for B, S, Cu, Zn, and Pb, which vary considerably in abundance, with no observed correlation to stratigraphy or silica content. Furthermore, no chemical distinction is observed between the subset of tephra which hosts harzburgite xenoliths (LB2005L, LB2007L, LB2009L, LB2011L, LB2019L, LB2024L, LB2025L, and LB2027L) and one crustal xenolith (LB2023L) and those which do not host any xenoliths. The unusually high silica content of crustal xenolith LB2032C (82.9 wt. %) suggests that it samples the rhyolitic interior of the Pliocene shield. Mafic granulite xenolith LB2020C has major- and trace-element compositions closely matching that of the trachybasaltic tephra.

The two trachybasalts from Blockhouse Butte display similar major- and trace-element compositions to the Lorena Butte scoriae, with trace-element compositions closely following the average OIB composition. A comparison of the HSE pattern for the Lorena Butte scoria (LB2012L) with OIB show that the Lorena Butte melt has a generally similar pattern to Cook Island (Snortum et al., 2019) and Canary Island lavas (Day et al., 2010), which have been shown to represent low degrees of partial melting. The Lorena Butte, Blockhouse Butte, and possibly other lavas in Simcoe sample a similar degree of partial melting and fertile intraplate melt sources.

Chemical comparison between Lorena Butte and the CRBG over which the cone lies can provide insight into their magmatic history. Compared with the Steens and Imnaha basalts (Day et al., 2021)—two of the earliest members of the CRBG—the Lorena Butte trachybasalts follow the same general trace-element pattern except for greater enrichment in the most incompatible elements (**Figure S11**). The Lorena Butte trachybasalt where the HSE were analyzed displays generally lower HSE content and higher  $^{187}\text{Os}/^{188}\text{Os}$  than the Steens basalts (0.1292 to 0.1336), but has similar HSE contents (Day et al., 2021) and  $^{187}\text{Os}/^{188}\text{Os}$  (0.134 to 0.158; Chesley & Ruiz, 1998) as the Imnaha basalts (**Figure S11**). Subsequent Grande Ronde and Wanapum members of the CRBG have progressively higher  $^{187}\text{Os}/^{188}\text{Os}$ , which has been proposed to be evidence for increased crustal mixing with the upwelling asthenosphere (Chesley & Ruiz, 1998). Since the Lorena Butte HSE and Os isotope systematics follow that of the Imnaha basalts, the magmatic history of Lorena Butte and plausibly that of the Simcoe Mountains volcanic field can be explained by a similar process where crustal material assimilates with upwelling melt as it extrudes to the surface.

## REFERENCES

- Abbey, S. (1983). Studies in "standard samples" of silicate rocks and minerals, 1969-1982. Papers - Geological Survey of Canada, 83-15, 1-114.
- Becker, H., & Dale, C. W. (2016). Re-Pt-Os isotopic and highly siderophile element behavior in oceanic and continental mantle tectonites. *Reviews in Mineralogy & Geochemistry*, 81, 369–440.
- Birck, J. L., Roy Barman, M., & Capmas, F. (1997). Re-Os isotopic measurements at the femtomole level in natural samples. *Geostandards Newsletter*, 20(1), 19-27.
- Birner, S. K., Cottrell, E., Warren, J. M., Kelley, K. A., & Davis, F. A. (2018). Peridotites and basalts reveal broad congruence between two independent records of mantle  $fO_2$  despite local redox heterogeneity. *Earth and Planetary Science Letters*, 494, 172-189.
- Boyd, F. R., & Mertzman, S. A. (1987). Composition and structure of the Kaapvaal lithosphere, southern Africa. *Magmatic Processes: Physicochemical Principles: Geochemical Society Special Publications*, 1, 13-24.
- Brandon, A. D., & Draper, D. S. (1996). Constraints on the origin of the oxidation state of mantle overlying subduction zones: An example from Simcoe, Washington, USA. *Geochimica et Cosmochimica Acta*, 60(10), 1739-1749.
- Brandon, A. D., Becker, H., Carlson, R. W., & Shirey, S. B. (1999). Isotopic constraints on time scales and mechanisms of slab material transport in the mantle wedge: evidence from the Simcoe mantle xenoliths, Washington, USA. *Chemical Geology*, 160, 387-407.
- Brandon, A. D., Creaser, R. A., Shirey, S. B., & Carlson, R. W. (1996). Osmium recycling in subduction zones. *Science*, 272(5263), 861-864.
- Brey G. P., & Kohler, T. (1990). Geothermobarometry in four-phase lherzolites II. New thermobarometers, and practical assessment of existing thermobarometers. *Journal of Petrology*, 31(6), 1353-1378.
- Chesley, J. T., & Ruiz, J. (1998). Crust-mantle interaction in large igneous provinces: Implications from Re-Os isotope systematics of the Columbia River flood basalts. *Earth and Planetary Science Letters*, 154, 1–11.
- Cohen, A. S., & Waters, F. G. (1996). Separation of osmium from geological materials by solvent extraction for analysis by thermal ionisation mass spectrometry. *Analytica Chimica Acta*, 332, 269-275.
- Davis, F. A., Cottrell, E., Birner, S. K., Warren, J. M., & Lopez, O. G. (2017). Revisiting the electron microprobe method of spinel-olivine-orthopyroxene oxybarometry applied to spinel peridotites. *American Mineralogist*, 102, 421-435.
- Day, J.M.D., & Walker, R. J. (2015). Highly siderophile element depletion in the Moon. *Earth and Planetary Science Letters*, 423, 114-124.
- Day, J.M.D., Nutt, K.L.R., Mendenhall, B., Peters, B. J. (2021). Temporally variable crustal contributions to primitive mantle-derived Columbia River Basalt Group magmas. *Chemical Geology*, 572.
- Day, J.M.D., Pearson, D. G., Macpherson, C. G., Lowry, D., & Carracedo, J. C. (2010). Evidence for distinct proportions of subducted oceanic crust and lithosphere in HIMU-type mantle beneath El Hierro and La Palma, Canary Islands. *Geochimica et Cosmochimica Acta*, 74(22), 6565-6589.
- Day, J.M.D., Walker, R. J., & Warren, J. M. (2017).  $^{186}\text{Os}$ – $^{187}\text{Os}$  and highly siderophile element abundance systematics of the mantle revealed by abyssal peridotites and Os-rich alloys. *Geochimica et Cosmochimica Acta*, 200, 232–254.



- Day, J.M.D., Waters, C. L., Schaefer, B. F., Walker, R. J., & Turner, S. (2016). Use of hydrofluoric acid desilicification in the determination of highly siderophile element abundances and Re-Pt-Os isotope systematics in mafic-ultramafic rocks. *Geostandards and Geoanalytical Research*, 40(1), 49-65.
- Downes, G. (2001). Formation and modification of the shallow sub-continental lithospheric mantle: a review of geochemical evidence from ultramafic xenolith suites and tectonically emplaced ultramafic massifs of western and central Europe. *Journal of Petrology*, 42(1), 233-250.
- Droop, G. T.R. (1987). A general equation for estimating  $\text{Fe}^{3+}$  concentrations in ferromagnesian silicates and oxides from microprobe analyses, using stoichiometric criteria. *Mineralogical Magazine*, 51, 431-435.
- Frost, B. R. (1991). Introduction to oxygen fugacity and its petrologic importance. *Reviews in Mineralogy and Geochemistry*, 25, 1-9.
- Govindaraju, K. (1994). Compilation of working values and sample description for 383 geostandards. *Journal of Geostandards and Geoanalysis*, 18, 158.
- Hildreth, W., & Fierstein, J. (2015). Geologic map of the Simcoe Mountains Volcanic Field, main central segment, Yakama Nation, Washington. U.S. Geological Survey.
- Jianping, L., Kornprobst, J., Vielzeuf, D., & Fabries, J. (1995). An improved experimental calibration of the olivine-spinel geothermometer. *Chinese Journal of Geochemistry*, 14(1), 68-77.
- Leeman, W. P., Smith, D. R., Hildreth, W., Palacz, Z., & Rogers, N. (1990). Compositional diversity of late Cenozoic basalts in a transect across the southern Washington Cascades: Implications for subduction zone magmatism. *Journal of Geophysical Research*, 95(B12), 19561-19582.
- Mattioli, G. S., & Wood, B. J. (1988). Magnetite activities across the  $\text{MgAl}_2\text{O}_4\text{-Fe}_3\text{O}_4$  spinel join, with application to thermobarometric estimates of upper mantle oxygen fugacity. *Contributions to Mineralogy and Petrology*, 98, 148-162.
- McDonough, W. F., & Sun, S.-s. (1995). The composition of the Earth. *Chemical Geology*, 120, 223-253.
- Mertzman, S. A. (2000). K-Ar results from the southern Oregon-northern California Cascade Range. *Oregon Geology*, 62(4), 99-102.
- Sack, R. O., & Ghiorso, M. S. (1991a). An internally consistent model for the thermodynamic properties of Fe-Mg-titanomagnetite-aluminate spinels. *Contributions to Mineralogy and Petrology*, 106, 474-505.
- Sack, R. O., & Ghiorso, M. S. (1991b). Chromian spinels as petrogenetic indicators; thermodynamics and petrological applications. *American Mineralogist*, 76, 827-847.
- Secchiari, A., Gleissner, P., Li, C., Goncharov, A., Milke, A., Becker, H., Bosch, D., & Montanini, A. (2020). Highly siderophile and chalcophile element behaviour in abyssal-type and supra-subduction zone mantle: New insights from the New Caledonia ophiolite. *Lithos*, 354-355.
- Snortum, E., & Day, J.M.D. (2020). Forearc origin for Coast Range Ophiolites inferred from osmium isotopes and highly siderophile elements. *Chemical Geology*, 550.
- Snortum, E., Day, J.M.D., & Jackson, M. G. (2019). Pacific lithosphere evolution inferred from Aitutaki mantle xenoliths. *Journal of Petrology*, 60(9), 1753-1772.
- Sun, S.-s., & McDonough, W. F. (1989). Chemical and isotopic systematics of oceanic basalts: implications for mantle composition and processes. Geological Society, London, Special Publications, 42(1), 313-345.

- Uto, K., Hildreth, W., & Lanphere, M. (1991). Geology, geochemistry and geochronology of the southern half of the Simcoe Mountains volcanic field, Washington. *Eos, Transactions of American Geophysical Union*, 72, 521.
- Wood, B. J., & Banno, S. (1973). Garnet-orthopyroxene and orthopyroxene-clinopyroxene relationships in simple and complex systems. *Contributions to Mineralogy and Petrology*, 42, 109-124.
- Wood, B. J., & Virgo, D. (1989). Upper mantle oxidation state: Ferric iron contents of lherzolite spinels by  $^{57}\text{Fe}$  Mössbauer spectroscopy and resultant oxygen fugacities. *Geochimica et Cosmochimica Acta*, 53, 1277–1291.
- Wood, B. J., Bryndzia, L. T., & Johnson, K. E. (1990). Mantle oxidation state and its relationship to tectonic environment and fluid speciation. *Science*, 248(4953), 337-345.

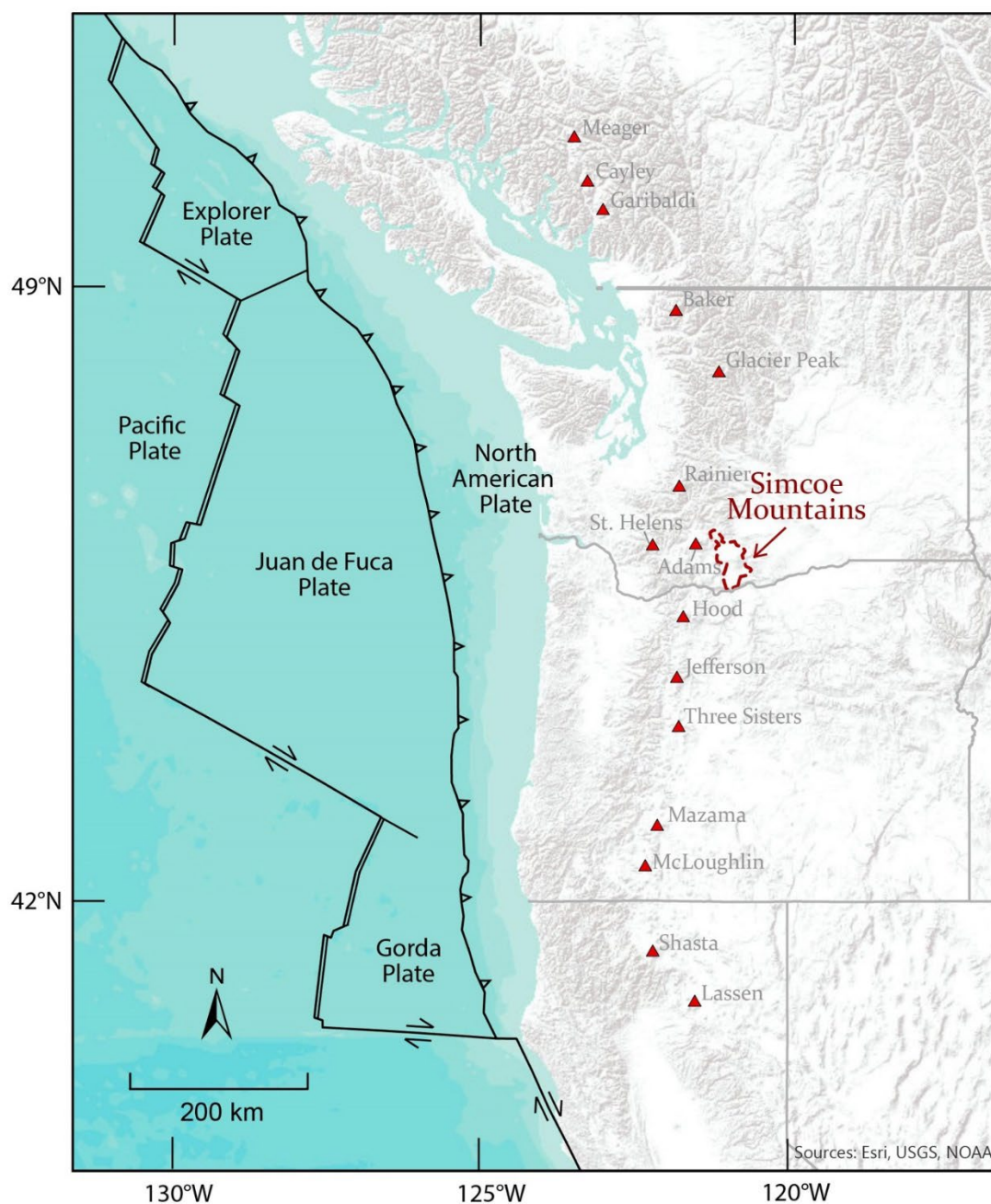


**Figure S1** – Tectonic setting of the study is within the Cascade arc. The Simcoe Mountains volcanic field lies in southern Washington just east of the Cascade arc axis, which is defined by the chain of stratovolcanoes and volcanic centers marked by red triangles. Dotted area denotes the Simcoe Mountains volcanic field. Modified after [Hildreth and Fierstein \(2015\)](#).

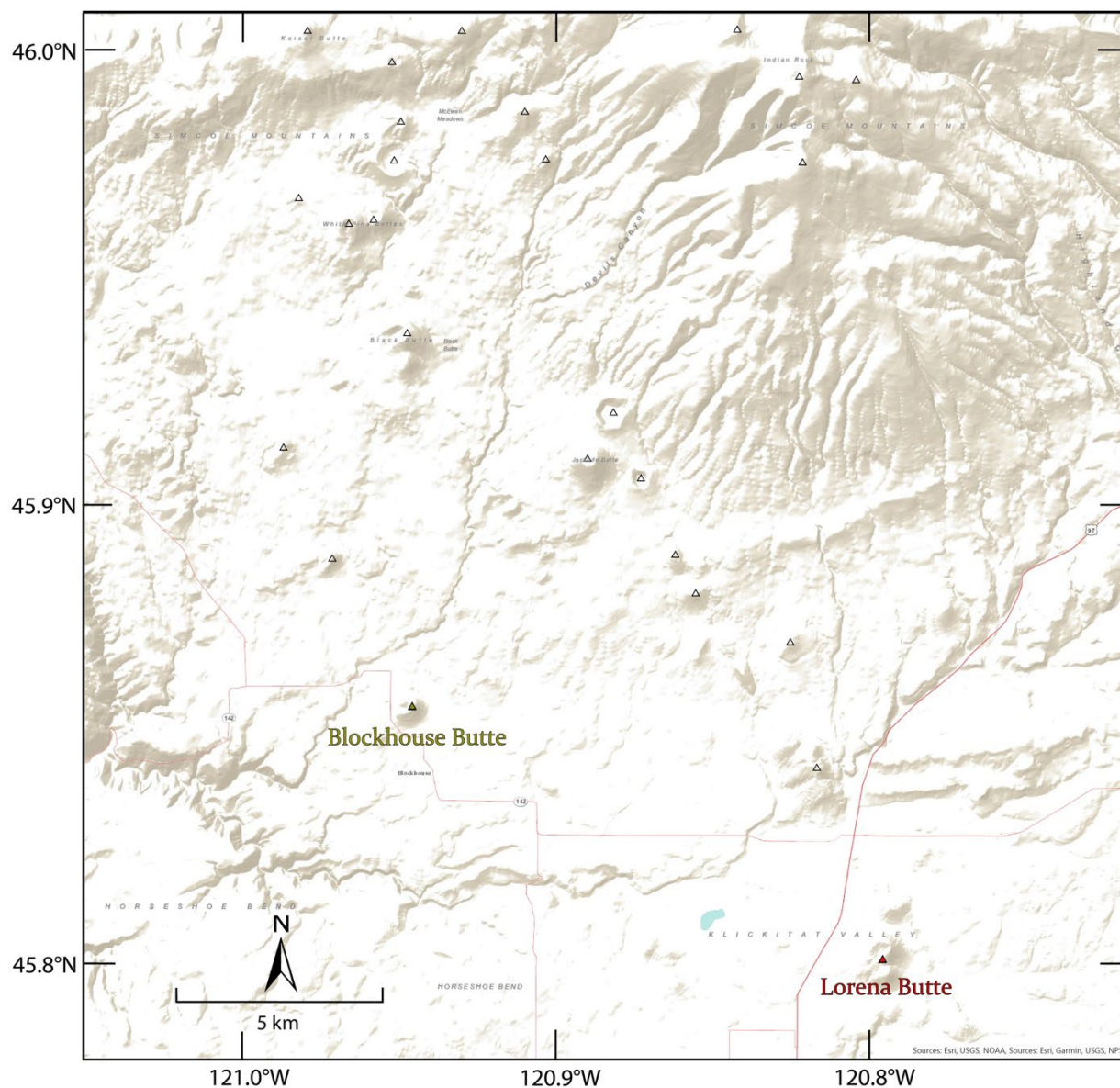


**Figure S2** - Terrain map of the southern section of Simcoe Mountains volcanic field showing the locations of Lorena Butte and Blockhouse Butte. The shield-like edifice spans the northwestern quarter of the map. Scattered cones and vents likely associated with the shield are marked by triangles.



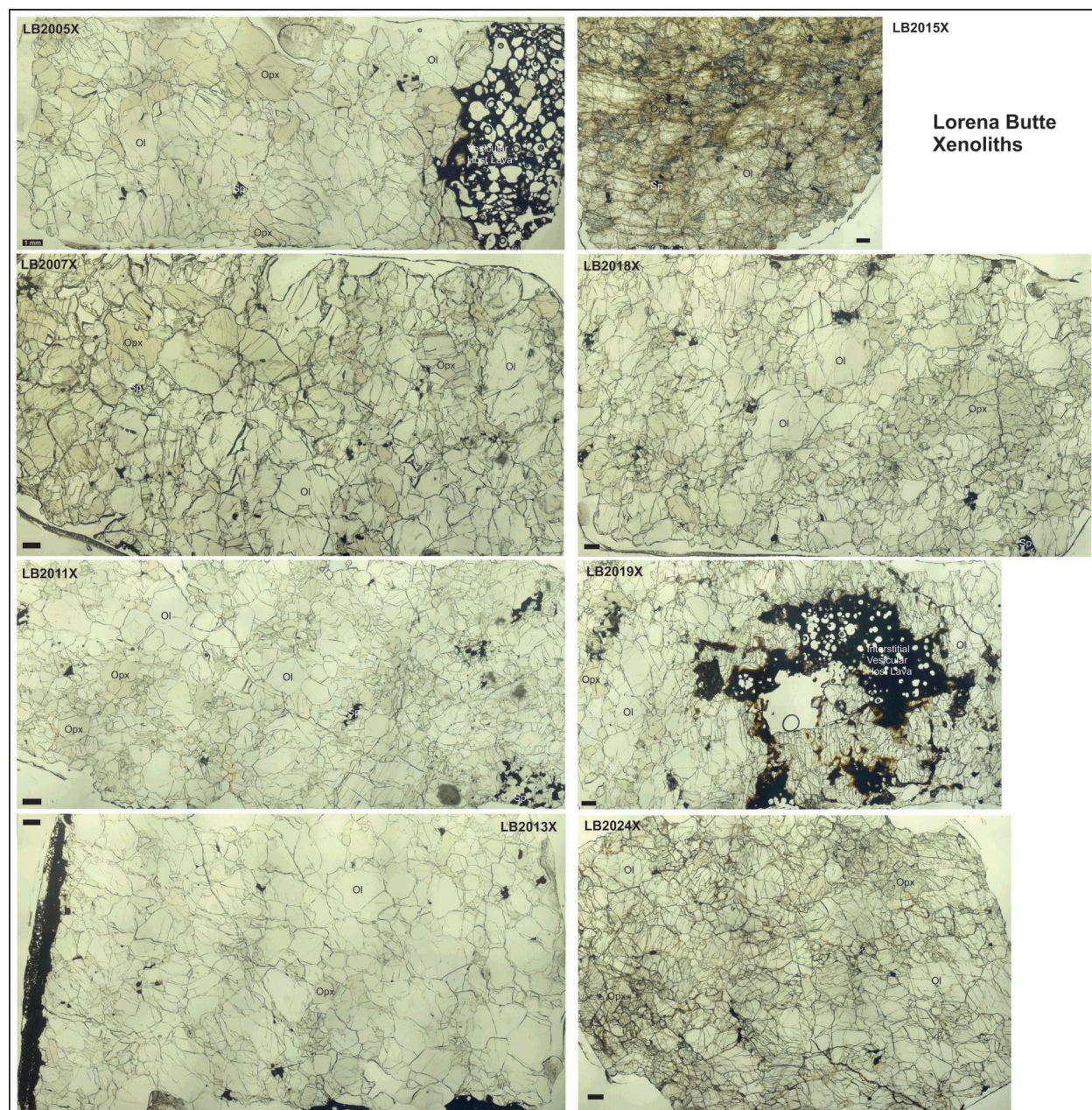


**Figure S3** – Photomosaic maps in plane polarized light of Lorena Butte xenoliths LB2005X, LB2007X, LB2011X, LB2013X, LB2015X, LB2018X, LB2019X and LB2024X. Scale bars are all 1 mm and olivine (Ol), orthopyroxene (Opx) and spinel (Sp) are all highlighted with other host lava features. Note that for whole rock analyses, basaltic selvages, and regions of obvious melt infiltration (e.g., LB2019X) were avoided – these features are shown for illustrative purposes.

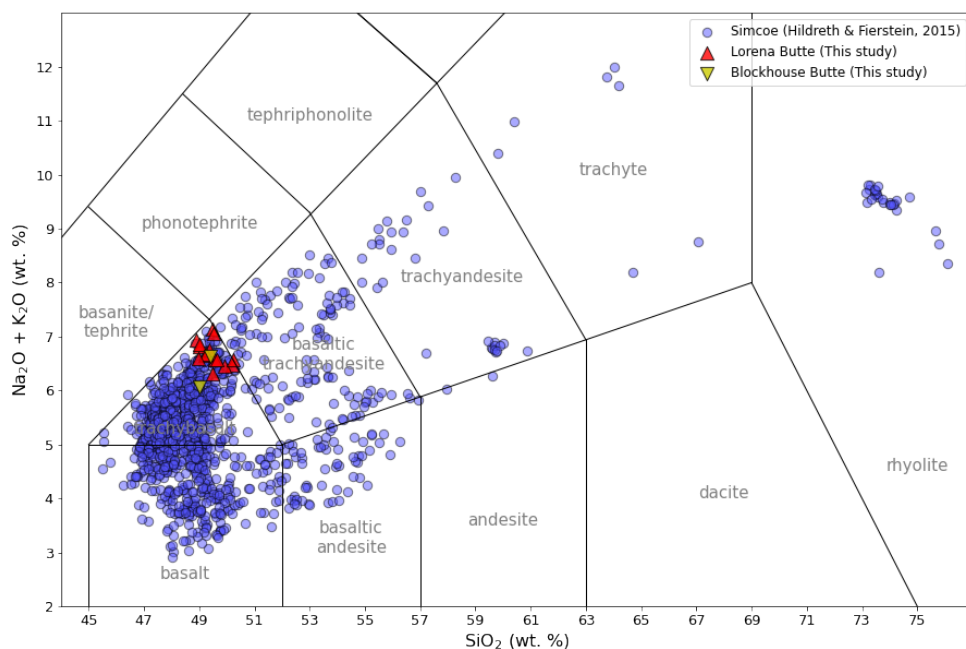


**Figure S4** - Total alkali versus silica plot of volcanic rocks from Lorena Butte (red triangle), Blockhouse Butte (yellow upside-down triangle), and Simcoe Mountains volcanic field (blue circles). Simcoe data are from [Hildreth & Fierstein \(2015\)](#). Transparency setting for data symbology is set to 20% for the Lorena Butte and Blockhouse Butte data symbology and 50% for Simcoe data to highlight overlapping data.

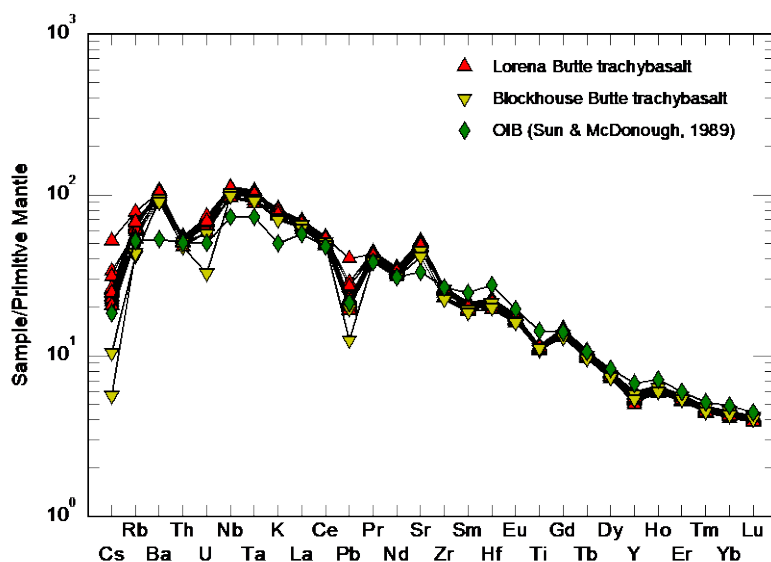


**Figure S5** - Lorena Butte and Blockhouse Butte trachybasalt whole-rock incompatible trace element concentrations. The trachybasalt trends closely follow the OIB trend after [Sun & McDonough \(1989\)](#). PM normalizations from [McDonough & Sun \(1995\)](#).



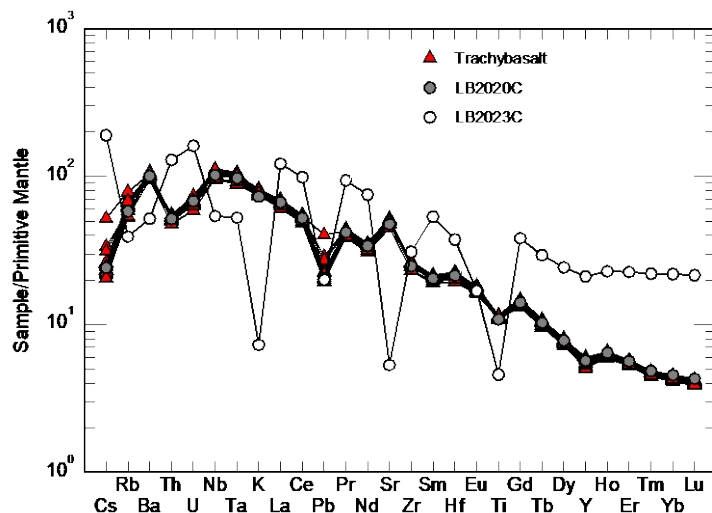


**Figure S6** - Whole-rock incompatible trace-element concentrations of Lorena Butte crustal xenoliths. Mafic granulite LB2020C follows the same trend as the trachybasalts, while rhyolitic sample LB2023 follows a different trend with variable enrichment or depletion in fluid-mobile elements and elevated REE. PM normalizations from [McDonough & Sun \(1995\)](#).

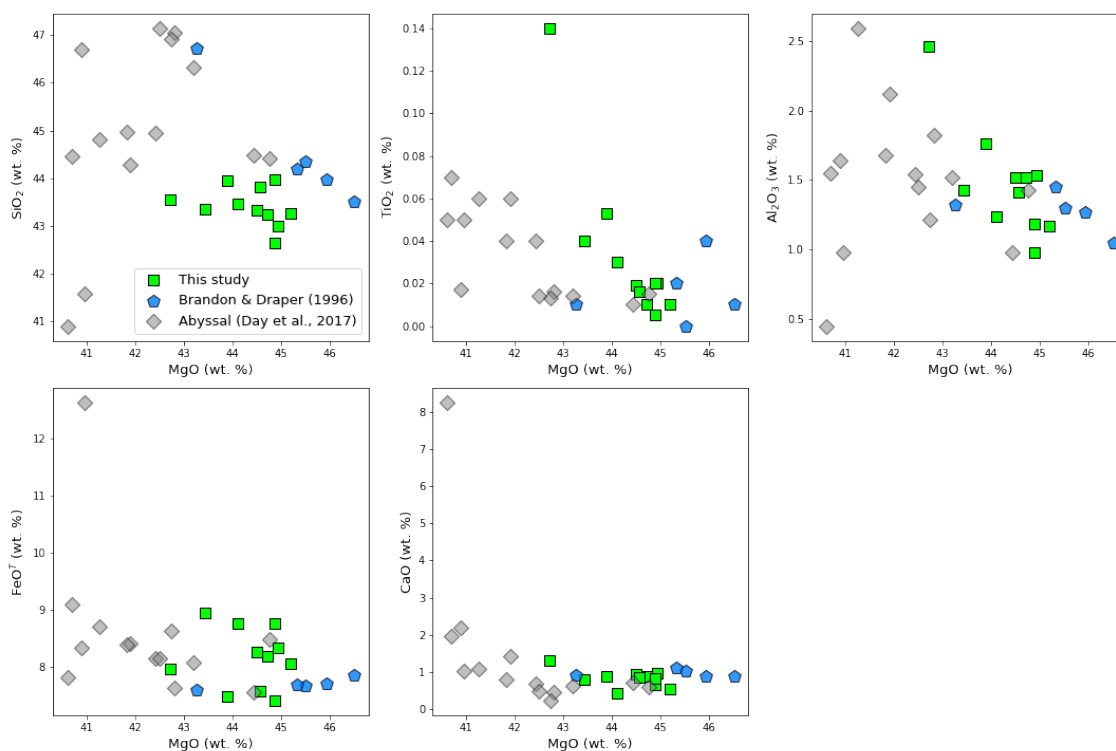


**Figure S7** - Major elements versus MgO in Lorena Butte harzburgites from this study and [Brandon & Draper \(1996\)](#) represented by green squares and blue pentagons, respectively, with 20% transparency. For comparison, abyssal harzburgites from [Day et al. \(2017\)](#) are plotted as grey diamonds with 50% transparency. Total  $\text{Fe}_2\text{O}_3$  from XRF analyses is recalculated as total FeO by dividing by 1.1111.

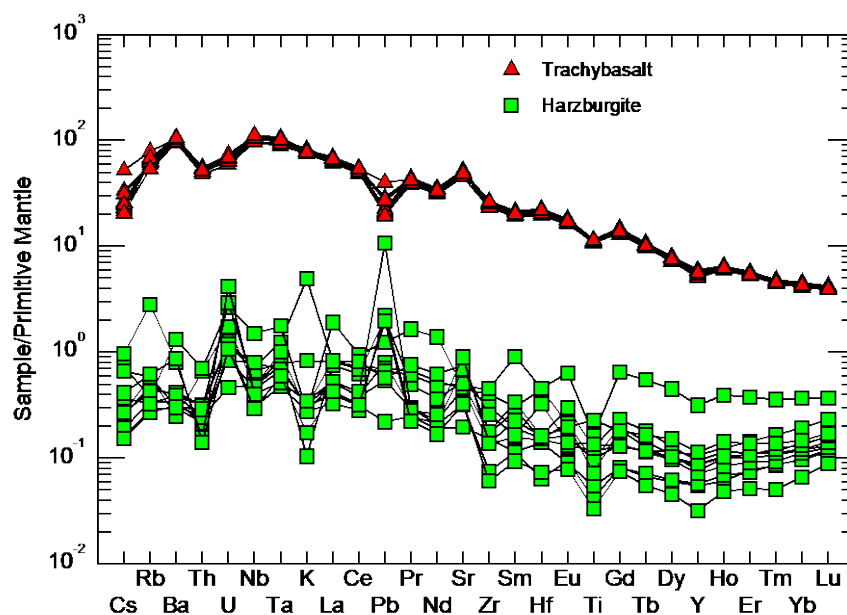


**Figure S8** - Lorena Butte harzburgites and trachybasalts whole-rock incompatible trace element concentrations. The harzburgites follow the general inflection pattern of the trachybasalts, which is interpreted to reflect refertilization of the incompatible trace element peridotites with the melt. PM normalizations from [McDonough & Sun \(1995\)](#).

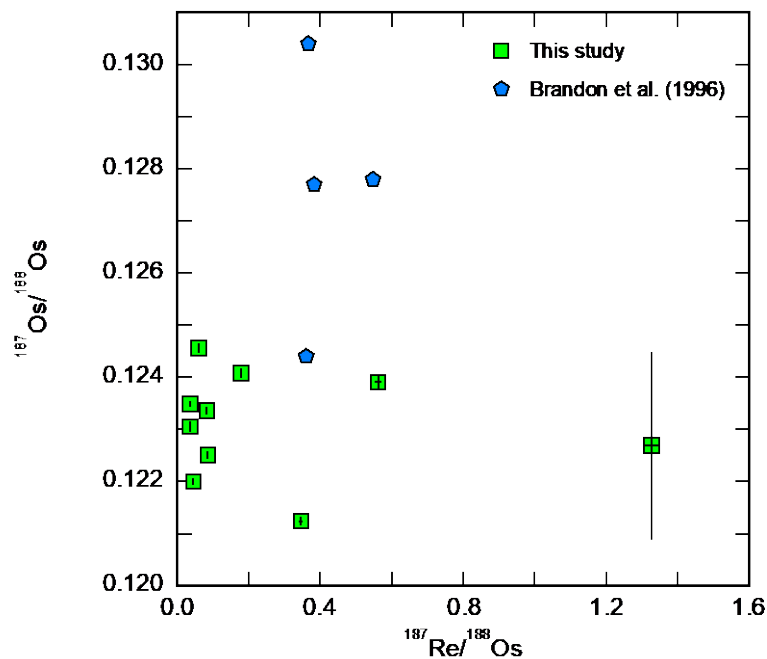


**Figure S9** - Lorena Butte harzburgite Os isotope systematics. Measured  $^{187}\text{Os}/^{188}\text{Os}$  for this study (green squares) is lower than that of [Brandon et al. \(1996\)](#) (blue pentagons). Error bars as shown for this study are generally smaller than symbol size, except for  $^{187}\text{Os}/^{188}\text{Os}$  in LB2007X.

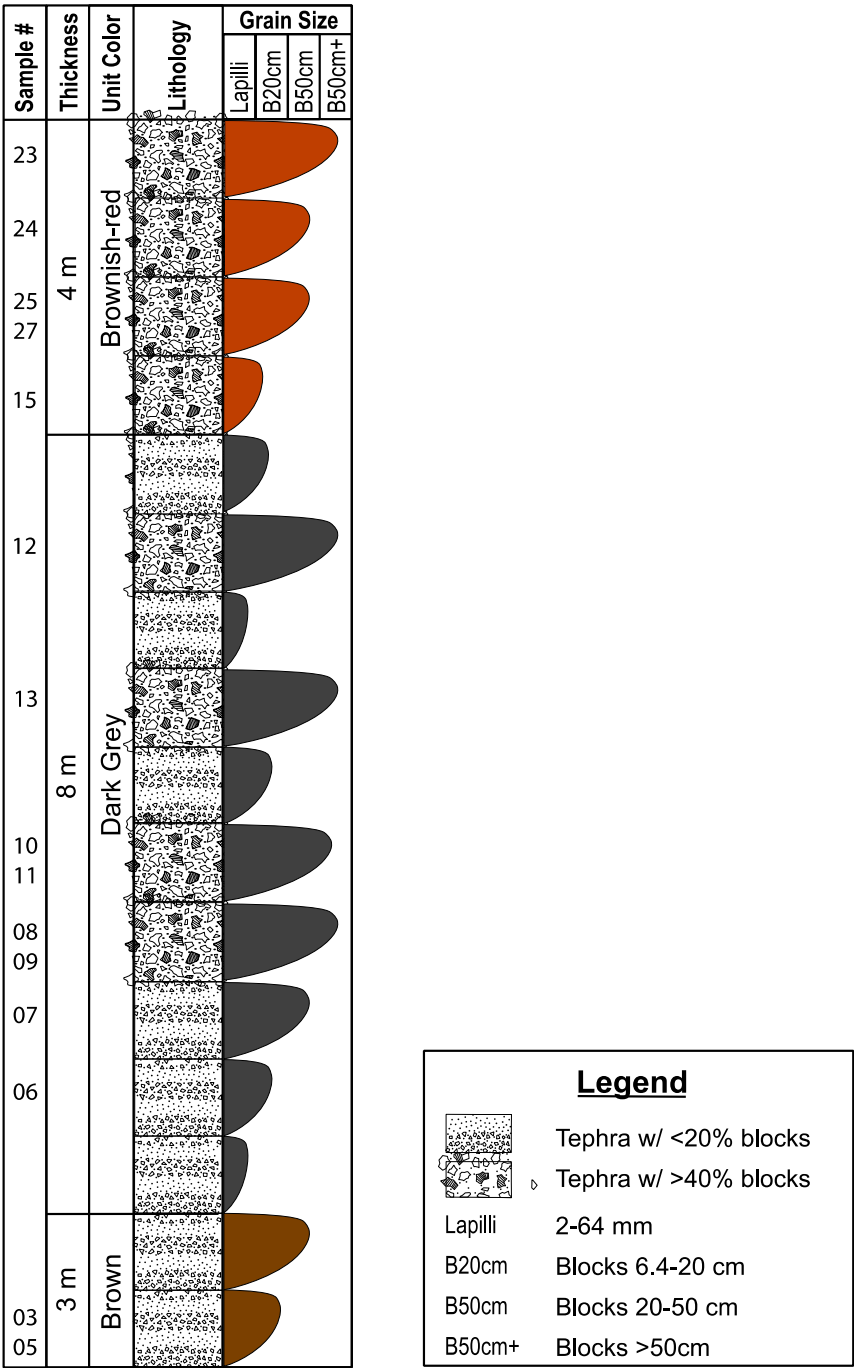


**Figure S10** - Simplified ~15-meter vertical section of Lorena Butte showing relative stratigraphic positioning of samples. The sample numbers shown are the last two digits of the scoria samples (e.g., sample #23 is LB2023L). Thicknesses of strata are approximate and not to scale.

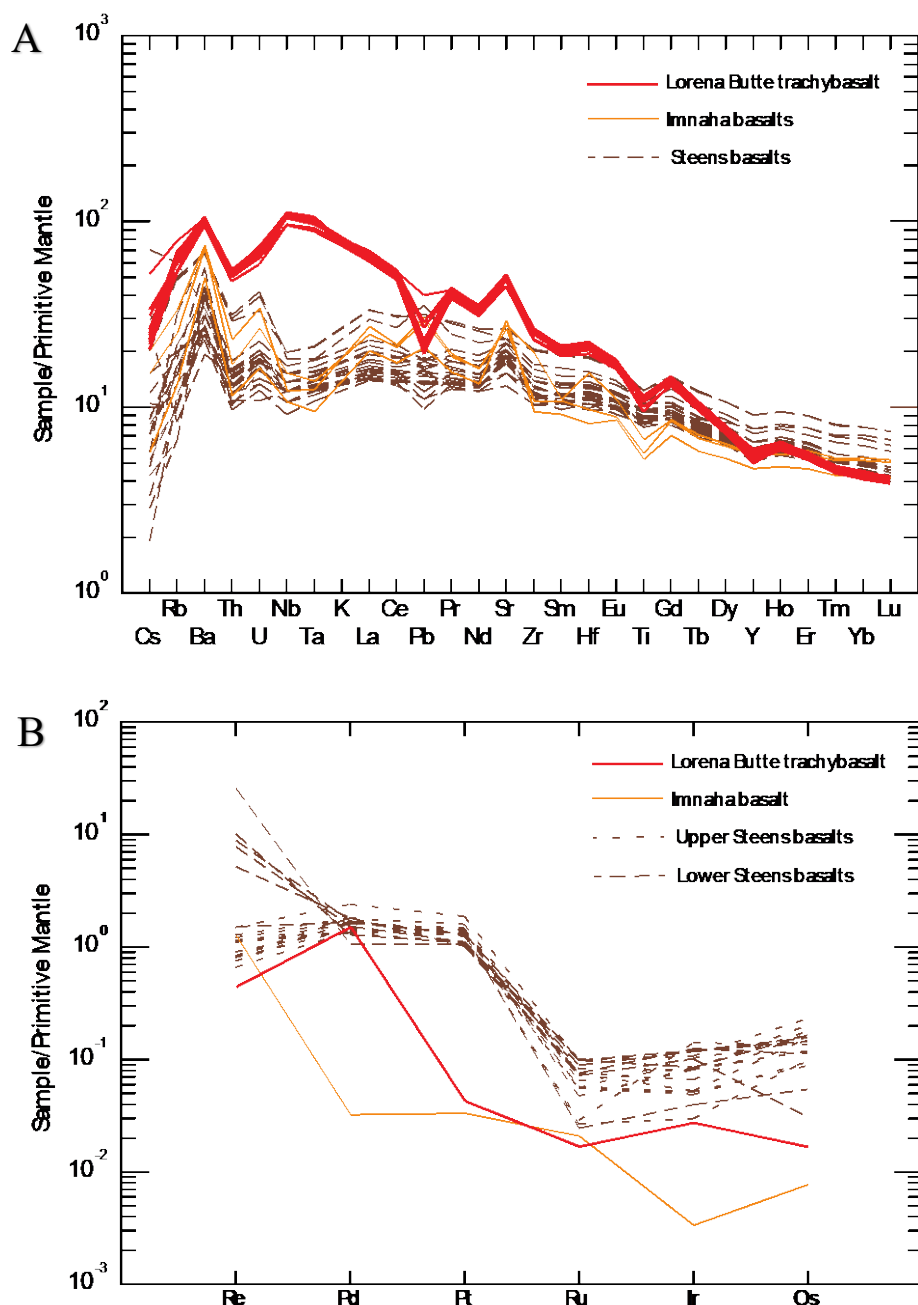


**Figure S11** – (a) Incompatible trace element and (b) highly siderophile element patterns of the Lorena Butte trachybasalts versus Steens and Innaha members of the CRBG. The trend of the trachybasalts generally follows that of Steens and Innaha basalts (from [Day et al., 2021](#)) with greater abundances of more incompatible elements, as expected with the greater degree of melting associated with flood-basaltic volcanism. Decreasing HSE abundances from Upper Steens, Lower Steens, to Innaha basalts can be explained by increased mixing with crustal components. The trachybasalt HSE trend generally follows that of the Innaha basalt, suggesting a similar intermixing of crustal components with an intraplate melt. PM normalization after [McDonough and Sun \(1995\)](#).

## SUPPLEMENTARY TABLES

Ten supplementary tables are available as excel spreadsheets and are as follows:

Table S1 - Major and trace element data for Lorena Butte and Blockhouse Butte trachybasalts.

Table S2 - Major and trace element data for Lorena Butte harzburgites and crustal xenoliths.

Table S3 - Standard Reference Materials used for trace element abundance analyses (values in ppm).

Table S4 - Analyses of olivine grains in Lorena Butte harzburgite xenoliths (wt.%).

Table S5 - Analyses of orthopyroxene grains in Lorena Butte harzburgite xenoliths (wt.%).

Table S6 - Analyses of clinopyroxene grains in Lorena Butte harzburgite xenoliths (wt.%).

Table S7 - Analyses of spinel grains in Lorena Butte harzburgite xenoliths (wt.%).

Table S8 - Geothermometry and oxygen fugacity calculations.

Table S9 - Full EPMA runs with standards (wt.%).

Table S10 - Parameters used for HSE model in Figure 1b.